N-Path Filtering and Mixing Analysis-A General Approach Based on Fourier Transform

Florence Podevin, Imadeddine Bendjeddou, Fadel Mohsen, Catalin Andrei Dobrin, Sana Ibrahim, Ali Alshakoush, Mamadou Diallo, Jordan Corsi, Loïc Vincent, Manuel Barragan, et al.

N-Path Filtering and Mixing Analysis - A General Approach Based on Fourier Transform

F. Podevin, *Member, IEEE*, I. Bendjeddou, F. Mohsen, C. A. Dobrin, S. Ibrahim, A. Al Shakoush, M. Diallo, J. Corsi, L. Vincent, M. J. Barragan, *Member, IEEE*, S. Bourdel, *Member, IEEE*

***Abstract*—This article proposes a general approach to accurately model the N-path filters and mixers, with the double purpose of bringing a better insight in the frequency transposition phenomena and opening the door towards a more general discussion concerning NPF-NPM and their outstanding properties as passive circuits. Thanks to a Fourier transform analysis, some mathematical equations are rigorously derived for both filtering and mixing voltage gains. The analysis is compared with ideal simulations for various sets of parameters: source impedance R_a, load impedance R_L, switch resistance R_{sw}, capacitive path C_L. Some error curves are extracted validating the initial hypotheses for the model in a given range of capacitances values. As a proof of concept, it is shown that the model complies with the measurements results with very good accuracy. The error is less than 10.5$\%$ on the two first harmonics prediction.**

***Index Terms*—N-path mixer, N-path filter, bandpass filter, switching circuit, LTI model.**

I. Introduction

FOR the last fifteen years, N-path filters and mixers (NPF-NPM) have been spreading worldwide, enabling a one-block solution to tunable passive filtering and mixing functions [1], [2]. Due to its passive nature, N-path circuits opened the door to very low power circuits for energy-efficient receivers such as wake-up radios [3] or Bluetooth low energy systems [4]. Thanks to their inherent reconfigurability, N-path architectures also allow for seamless operation across different target standards. Moreover, the introduction of harmonic rejection N-path mixers (HR-NPM) [5] makes these structures very suitable for the implementation of efficient widely tunable receivers. For software-design radios (SDR), HR-NPM architectures feature in the same block both mixing and filtering of the RF signal coming from the antenna [5], contrarily to conventional wideband SDR, as in [6] or in [7], where filtering and mixing functions are performed through two distinct blocks.

The fields of investigation for N-path are many-fold. In mixer-first architectures, matching to the antenna is a key constraint in the design [8], among others as low noise [9] and high linearity [10]. In LNA-first architectures, antenna matching is performed by the LNA but there exists other key design constraints. As an example, for HR-NPM, tolerance to blockers [11] and low circuit complexity [12], [13], are also targeted. If we focus now on the two main functions of an NPF-NPM, addressing the design of an N-path structure requires defining its input impedance (targeting matching to source or, contrarily, operating in high-impedance mode), specifying its RF and IF bandwidths, and enhancing its conversion gain. In this regard, the development of a simple model for N-path circuit that captures its behavior, including both source and load impedances in order to predict accurately its input impedance, filtering and mixing responses, is of key importance for the design and understanding of these structures. Such model aims at proposing a linear time-invariant (LTI) behavior equivalent to the dynamic linear time varying (LTV) behavior of the N-path. For better understanding, Fig.1.a and Fig.1.b provide an example of N-path with $N = 4$ showing the LTV circuit and its common representation split in two blocks: the filtering block with an LTI model consisting of an RLC circuit followed by a mixing block represented from a functional point-of-view.

A first example of such model was proposed in 2010, in [14], deriving the transposition of the low-pass baseband filtering response $R_L C_L$ (see Fig.1.a) towards high frequency. In [14], for the very first time, the source impedance R_a and the load impedance R_L dynamic transpositions were considered. However, the capacitive dynamic transfer was not taken into

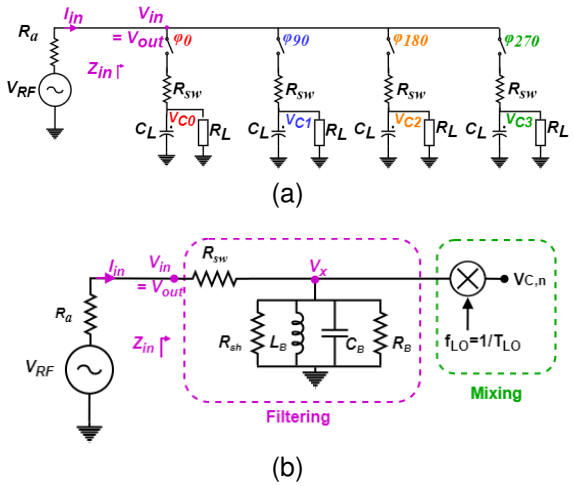

Fig. 1: Example of NPF with $N = 4$. a) LTV circuit. b) 2-block representation at fundamental frequency, LTI model with RLC circuit for filtering and functional block for mixing. The switch resistance has been represented as R_{sw}.

All authors are with the TIMA laboratory, Unité Mixte de Recherche 5159 CNRS, Univ. Grenoble Alpes, Grenoble Institute of Technology, Grenoble, France (FirstName.LastName@univ-grenoble-alpes.fr).

This work has been funded by the European Union under Project: 101070287 - SWAN-on-chip - HORIZON - CL4 - 2021 - DIGITAL - EMERGING - 01

Manuscript received Sept 2023

account. This aspect was included in 2015 by the same team, in [15], that employed a time-domain approach to derive a quasi-complete model integrating both shunt antenna, R_{sh}, i.e., the transposition of R_a, dynamic baseband load impedance, R_B, i.e. the transposition of R_L and dynamic equivalent capacitance, C_B, i.e., the transposition of C_L. However, the model did not include a dynamic equivalent inductor in parallel to the dynamic capacitor, and consequently could not describe the observed bandpass RF filtering response. In [16], a similar model was proposed including both the dynamic inductor L_B and capacitor C_B, taking into account the shunt antenna impedance but, however, ignoring the load impedance of the mixer. This model was further enhanced in [17], where all relevant impedances in Fig. 1b. were considered. Nevertheless, the current convolution with load impedance is still not clearly highlighted. In this time-domain approach, only the behavior around fundamental frequency is explored. In [18], commented in [19], an interesting current-based approach was proposed in the frequency domain, introducing convolution between current and baseband impedance. This enables, among other advantages, to simply introduce an expression of the input impedance depending on the considered clock harmonic component. However, the derivation of the RF input impedance seen from the source side is simplified as it does not consider the shunt antenna impedance. This is of minor importance for large values of N, but might have an impact on the filtering and mixing gains for low values of N such as N =4. Currently, the models presented in [15] and [16] are still widely used, as in [20] where a stack of seven capacitors is used as a charge pump. A simple transformer is added in the proposed LTI model to take into account the voltage gain due to charge pump while including the antenna shunt impedance and the dynamic load resistance. However, as the filtering response is not under study, no LC network is represented.

In this work, we propose a simple model for the NPF-NPM behavior derived in its entirety in the frequency domain for arbitrary source and load impedances. The equivalent analytical model takes into consideration all the harmonic components of the clock signal which constitutes the main contribution of this work. This is of major interest in the context of HR-NPM or widely tunable receivers where some clock strategies can include harmonics use, as in [21]. From the filtering point-of-view, it will be shown that the behavior can be represented as an RLC filter. After reminding the principle of N-path filters or mixers in section 2, we analyze in section 3 the input impedance of the LTV NPF-NPM circuit, based on a simple Fourier transform approach, and validate a general harmonic-dependent LTI model, valid for an arbitrary load. A specific focus is made on antenna matching. In section 4, we provide a general expression for the filtering and mixing gains, discussed in section 5 on the basis of a number of different simulated application cases. Section 5 also includes some model error analysis to verify the accuracy of the model. Finally section VI validates the model with some measurement comparisons. Section VII concludes this work and provides some perspectives.

II. Principle of N-Path Mixer

NPF is an electronic circuit using N paths, materialized by N identical capacitors C_L. As illustrated on Fig.2.a and Fig.2.f, it consists in sampling, through a switch, at every period T_{LO} and during a time interval of T_{LO}/N, an RF signal $v_{RF}(t) = A(t)cos(2\pi f_{RF}t+\phi(t))$, where amplitude $A(t)$ and time varying phase $\phi(t)$ capture the modulation of the received signal.

From the receiver point-of-view, this modulation effect is considered in frequency domain as the transposition of a baseband signal, $V_{BB}(f)$, around a radio-frequency carrier, f_{RF}, as illustrated in [22], [23], which is written as:

$$V_{RF}(f) = V_{BB}(f) * \left(\frac{\delta(f - f_{RF}) + \delta(f + f_{RF})}{2} \right) \quad (1)$$

with $*$ the convolution product and $\delta(f - f_{RF})$ the Dirac peak at frequency f_{RF}.

Capacitor C_L is replenished only during the n^{th} time interval of width T_{LO}/N. The action is repeated N times per period, at each path, with a time delay between the switches clock signals of two consecutive paths equal to T_{LO}/N. If frequency f is close to $f_{LO} = 2\pi/T_{LO}$ then the signal is said in the filter bandwidth where center frequency is f_{LO}. In that way, NPF is very efficient to improve the rejection of non-desired signals (interferences due to blockers for example). If f is close to $kf_{LO} = 2\pi k/T_{LO}$ then the signal is still in a filter bandwidth, centered around kf_{LO} this time. Filtering response around kf_{LO} is represented in Fig.3.b.

The signal V_{in} in Fig.2 and represented in frequency domain in Fig.3, is the one after the source impedance R_a, at the circuit input node, where the input impedance Z_{in} is defined. NPF is particular in that sense that the RF output signal is also the RF input $V_{out}(f) = V_{in}(f)$. Impedance R_L stands for the load at the capacitors nodes, for example an output buffer input impedance. It is interesting to note that, at this capacitor node, the voltage $V_{c,n}(f)$ is a mixed version of the RF signal with the LO clock that samples the RF, as illustrated in Fig.3.c. For this reason, NPF inherently provides a mixing function and is irrespectively referred to as NPF or NPM in the literature and may be used for that purpose. Authors are considering R_L as a simple high resistive load for illustration and write $Z_L = C_L \| R_L$ in that precise case, but Z_L could be a more complex impedance as $C_L \| R_L(f) \| X_L(f)$ for example, leading to a higher order mode filtering.

For pedagogical aspects, and in order to exemplify the high selectivity behavior of the LTV circuit of Fig.2.a, its time varying response is plotted in Fig.4 where $v_{in}(t)$ and any $v_{c,n}(t)$ result from theoretical simulations with ideal components. The chronogram representation restricts $v_{RF}(t)$ to $Acos(2\pi f_{RF}t)$ with the purpose of better understanding. Once steady-state is reached, it is noteworthy that for $f_{RF} = f_{LO}$, $v_{c,n}(t)$ is almost constant except slight variations observed during on-switch slot. For $f_{RF} \sim f_{LO}$, $v_{c,n}(t)$ varies at intermediate frequency $f_{IF} = f_{RF} - f_{LO}$. Signal of frequency f_{RF} far from f_{LO} (or from any f_{LO} harmonics) is filtered. Lastly, for $f_{RF} = 2f_{LO}$, $v_{c,n}(t)$ tends to be almost constant once again with still some little glitches occurring while switch is on.

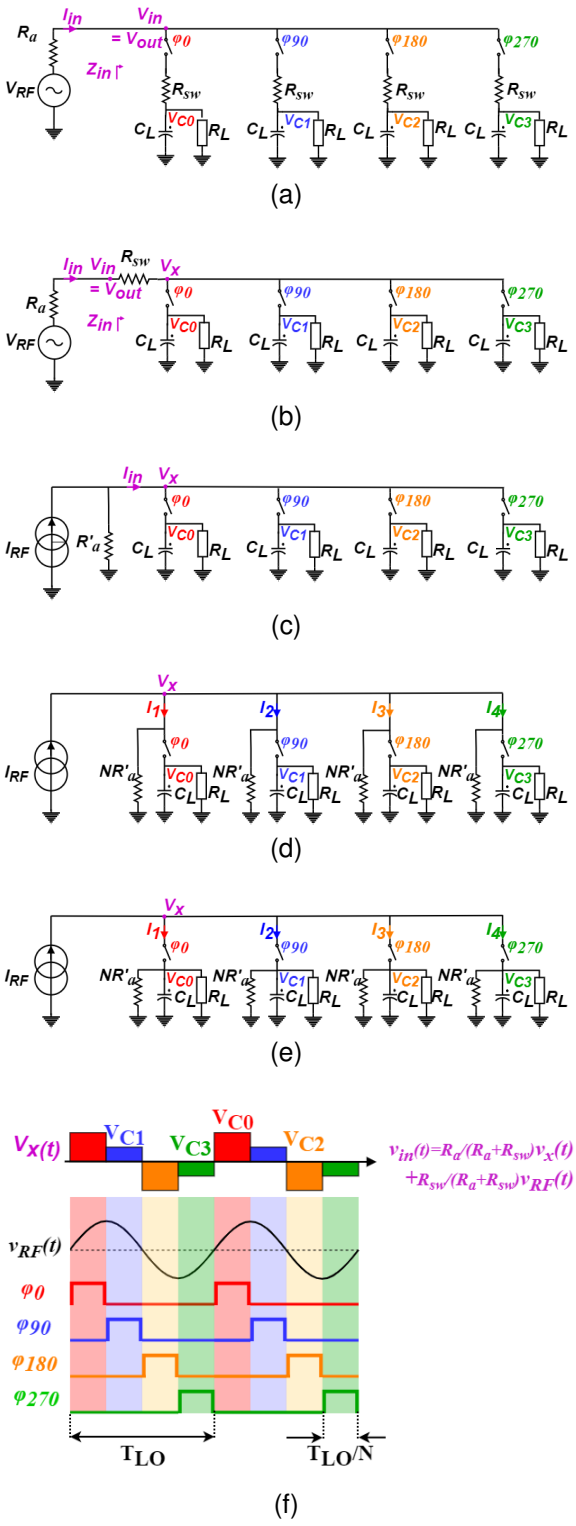

Fig. 2: Example of NPF with $N = 4$. Linear time varying model LTV. a) to d) Different ways to represent the same circuit. e) Quasi equivalent circuit. f) For the sake of simplicity, the chronogram representation restricts $v_{RF}(t)$ to $Acos(2\pi f_{RF}t)$. The switch resistance has been represented as R_{sw}.

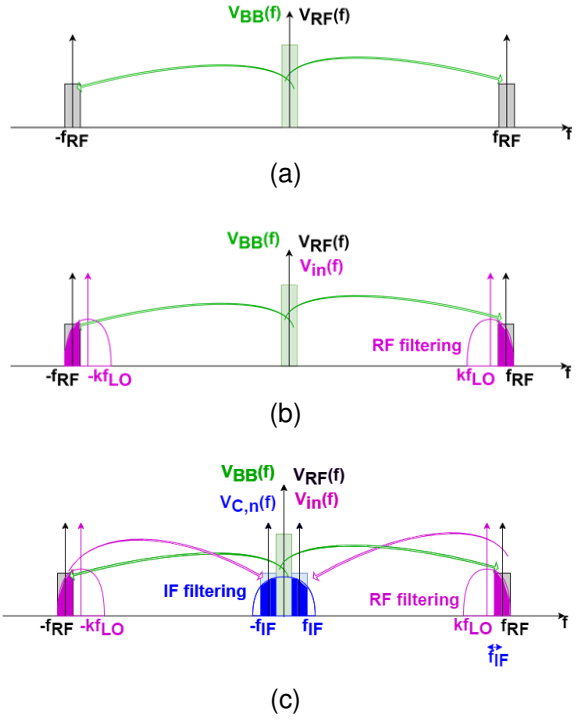

Fig. 3: Modulated RF and IF signals, as a transposition of BB signal and their filtering response.

III. Impedance analysis

A. Fourier transform approach

Authors are proposing a general demonstration of their model based on the schematics presented in Fig.2 associated with some mathematical derivations.

1) Extra parameters and methodology presentation:: Fig.2.b reproduces Fig.2.a where we define the virtual voltage $v_x(t)$ at the node in between R_{sw} and the switches, still considered as ideal. We define as well an effective resistance R'_a as a single lumped series combination of R_a and R_{sw}: $R'_a = R_a + R_{sw}$. An accurate way to analyse such network consists in performing RF signal processing through the various filtering and sampling functions, once steady state is reached. By introducing a Thevenin-Norton transformation, it becomes easy to calculate $v_x(t)$ in time domain by considering either current or voltage sampling, and then to transform equations from time to frequency domain.

2) Currents along paths, $i_n(t)$, and main hypotheses: Hence, Fig.2.c represents the Thevenin equivalent circuit of Fig.2.a whilst Fig.2.d shows the same approach where R'_a has been simply replaced by N parallel NR'_a. Fig.2.d is fully equivalent to Fig.2.a, so that we can define current $i_{RF}(t)$ as

$$i_{RF}(t) = \frac{v_{RF}(t)}{R'_a} \tag{2}$$

Leading to $I_{RF}(f)$ in frequency domain:

$$I_{RF}(f) = \frac{V_{BB}(f) * \left(\frac{\delta(f-f_{RF})+\delta(f+f_{RF})}{2}\right)}{R'_a} \tag{3}$$

We can now introduce the N currents $i_n(t)$. The first hypothesis is as follows: when the switch of the n^{th} cell is close, during the interval $[\frac{nT_{LO}}{N}; \frac{(n+1)T_{LO}}{N}]$, we consider that currents $i_{l\neq n}(t)$ present a negligible value as compared to $i_n(t)$. This is valid as long as we can assume a strong

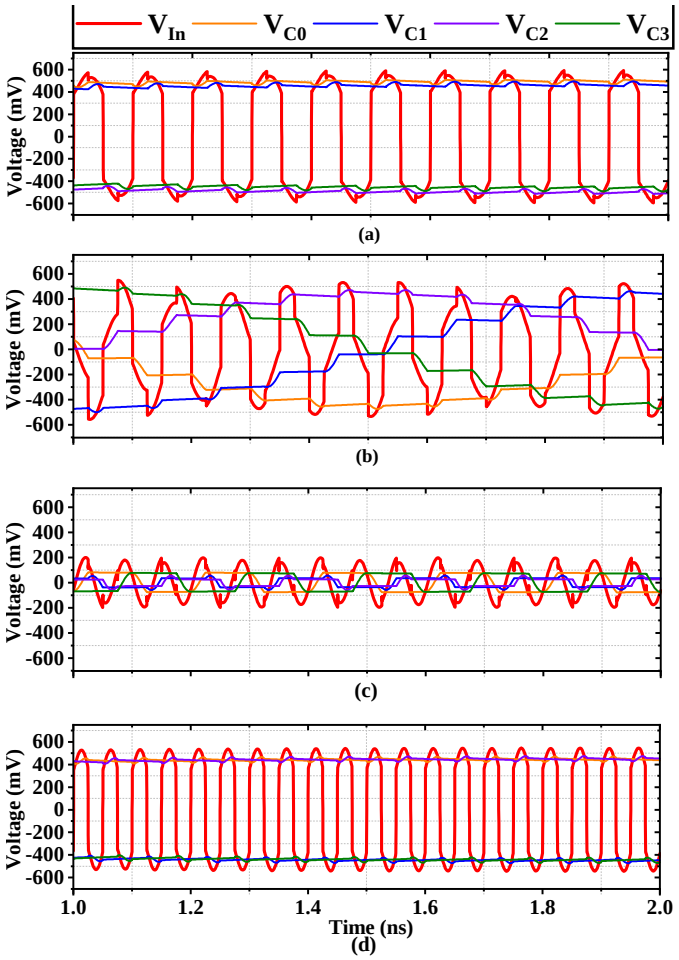

Fig. 4: LTV results for $N = 4$, $R_a = 50\ \Omega$, $R_{sw} = 10\ \Omega$, $R_L = 1\ k\Omega$, $C_L = 20$ pF, $f_{LO} = 1$ GHz. a) $f_{RF} = 1$ GHz. b) $f_{RF} = 1.05$ GHz. c) $f_{RF} = 1.5$ GHz. d) $f_{RF} = 2$ GHz.

capacitive RF path through C_L, meaning that first $\frac{1}{\omega C_L} \ll R_L$ which is most of the time the case with high input impedance buffers, and that second $\frac{1}{\omega C_L} \ll R'_a$ which is a more risky assumption when dealing with rather small antenna impedances. On the basis of this assumption, we can say that $i_n(t)$ is the time-windowed version of $i_{RF}(t)$ during the considered n^{th} slot. Also, once switch n is closed, during $\frac{T_{LO}}{N}$, C_L empties the accumulated charges through R'_a (the N parallel NR'_a) and its own R_L. Once switch n is open, C_L empties the accumulated charges through R_L only. Within the demonstration, the second hypothesis suggests that C_L can discharge completely in R'_a during the time slot $\frac{T_{LO}}{N}$, meaning that $R'_a C_L \ll \frac{T_{LO}}{N}$. That way, we can state that the discharge is a continuous discharge through R_L and NR'_a, leading to the quasi-equivalent circuit of Fig.2.e. The pertinence of both hypotheses will be checked afterwards in section V.C.

3) $v_x(t)$ and $V_x(f)$ calculation: We consider first $v_x(t)$ as the sum on n of the time-windowed versions of the various $v_{c,n}(t)$ as shown in Fig.2.f. This can be mathematically written as

$$v_x(t) = \sum_{n=0}^{N-1} \left(v_{c,n}(t) \cdot \left[w_{T_{LO}} \left(t - \frac{nT_{LO}}{N} \right) * \Pi_{\frac{T_{LO}}{N}}(t) \right] \right) \tag{4}$$

where $\Pi_{\frac{T_{LO}}{N}}(t)$ is a gate of width $\frac{T_{LO}}{N}$ centered around $t = 0$. This gate is convoluted around each Dirac peak of the Dirac comb $w_{T_{LO}}\left(t - \frac{nT_{LO}}{N}\right)$.
Fourier transform of $\Pi_{\frac{T_{LO}}{N}}(t)$ is $\frac{T_{LO}}{N} \cdot sinc(\pi f \frac{T_{LO}}{N})$.
Fourier transform of $w_{T_{LO}}\left(t - \frac{nT_{LO}}{N}\right)$ is $W_{f_{LO}}(f) \cdot e^{-j2\pi f n \frac{T_{LO}}{N}}$.
Gating is a shaping response corresponding to convolution in time domain leading to a product in frequency domain.

In parallel, from Fig.2.e, it can be stated that

$$v_{c,n}(t) = i_n(t) * z(t) \tag{5}$$

where $z(t)$ is the time representation of $Z(f)$ in frequency domain:

$$Z(f) = NR'_a \| Z_L(f) \quad (a) \tag{6}$$

$$Z(f) = \frac{NR'_a R_L}{NR'_a + R_L + j2\pi f NR'_a C_L R_L} \quad (b)$$

(6).a is the lowpass filter impedance, which response is represented on Fig.3.c. (6).b is the lowpass filter impedance of cutoff frequency $\frac{1}{2\pi C_L (NR'_a \| R_L)}$ when R_L is a simple high resistive load. Whatever low pass filter $Z(f)$, $v_x(t)$ is re-written as (7)

$$v_x(t) = \sum_{n=0}^{N-1} \{ [i_n(t) * z(t)] \cdot \left[w_{T_{LO}} \left(t - \frac{nT_{LO}}{N} \right) * \Pi_{\frac{T_{LO}}{N}}(t) \right] \} \tag{7}$$

Finally, we can express $i_n(t)$ as the sampled and hold version of $i_{RF}(t)$:

$$i_n(t) = i_{RF}(t) \cdot \left(w_{T_{LO}} \left(t - \frac{nT_{LO}}{N} \right) * \Pi_{\frac{T_{LO}}{N}}(t) \right) \tag{8}$$

From (7) and (8) in time domain, and as demonstrated in Appendix A, an explicit expression of $V_x(f)$ in frequency domain is given by (9)

$$V_x(f) = \sum_{k=-\infty}^{+\infty} \left\{ I_{RF}(f) \cdot \frac{1}{N} \cdot sinc^2 \left(\frac{k\pi}{N} \right) \cdot Z(f - kf_{LO}) \right\} \tag{9}$$

4) Input impedance Z_{in} calculation:

$$Z_{in}(f) = \frac{V_{in}(f)}{I_{in}(f)} \tag{10}$$

whilst $V_{in}(f)$ is obtained through the following voltage sum,

$$V_{in}(f) = V_x(f) + R_{sw} I_{in}(f) \tag{11}$$

and $I_{in}(f)$ is obtained through current node law,

$$I_{in}(f) = I_{RF}(f) - \frac{1}{R'_a} V_x(f) \tag{12}$$

so that $Z_{in}(f)$ can be developed as in (13).

$$Z_{in}(f) = R_{sw} + \frac{V_x(f))}{I_{RF}(f) - \frac{1}{R'_a}V_x(f)} \quad (a)$$

$$Z_{in}(f) = R_{sw} + \frac{\sum_{k=-\infty}^{+\infty}\left[\frac{1}{N}\cdot sinc^2\left(\frac{k\pi}{N}\right)\cdot Z(f-kf_{LO})\right]}{1-\frac{1}{R'_a}\sum_{k=-\infty}^{+\infty}\left[\frac{1}{N}\cdot sinc^2\left(\frac{k\pi}{N}\right)\cdot Z(f-kf_{LO})\right]} \quad (b) \tag{13}$$

The component of $Z_{in}(f)$ at $f \sim kf_{LO}$, namely $Z_{in}^{(k)}$, is edited synthetically through (14) and (15) where $\Delta f = f - kf_{LO}$.

$$Z_{in}^{(k)} = R_{sw} + \frac{\gamma_N^{(k)}\cdot Z(\Delta f)}{1-\frac{1}{R'_a}\cdot\gamma_N^{(k)}\cdot Z(\Delta f)} \tag{14}$$

We define here $\gamma_N^{(k)}$ by:

$$\gamma_N^{(k)} = \frac{1}{N}\cdot sinc^2\left(\frac{k\pi}{N}\right) \tag{15}$$

When $Z(f)$ is the basic impedance of (6).b, then:

$$Z_{in}^{(k)} = R_{sw} + \frac{\gamma_N^{(k)}\cdot NR'_aR_L}{NR'_a + R_L + j2\pi\Delta f\cdot NR'_aC_LR_L - \gamma_N^{(k)}\cdot NR_L} \tag{16}$$

B. Linear Time Invariant LTI model

Let's call

$$\begin{aligned} R_B^{(k)} &= \gamma_N^{(k)}R_L \\ C_B^{(k)} &= \frac{C_L}{2\gamma_N^{(k)}} \\ \alpha_N^{(k)} &= \frac{N\gamma_N^{(k)}}{1-N\gamma_N^{(k)}} \\ R_{sh}^{(k)} &= \alpha_N^{(k)}R'_a \end{aligned} \tag{17}$$

(16) is simplified when introducing the equivalent dynamic resistance $R_B^{(k)}$, the equivalent dynamic capacitor $C_B^{(k)}$, the shunt impedance $R_{sh}^{(k)}$, as demonstrated in Appendix B.

$$Z_{in}^{(k)} = R_{sw} + \frac{R_{sh}^{(k)}\|R_B^{(k)}}{1+j2\pi\cdot 2\Delta f\cdot C_B^{(k)}\left(R_{sh}^{(k)}\|R_B^{(k)}\right)} \tag{18}$$

(18) shows similarities with a combo of parallel resistances and resonating network at kf_{LO}: $Z_B^{(k)} = R_{sh}^{(k)}\|R_B^{(k)}\|C_B^{(k)}\|L_B^{(k)}$ in series with R_{sw}. One resistance is the source-dependant shunt resistance $R_{sh}^{(k)}$ whilst the other is the transposition of the load impedance through the N-path circuit $R_B^{(k)}$. Inductance is defined by $L_B^{(k)} = \frac{1}{(2\pi f_0)^2 C_B^{(k)}}$. It is worth mentioning that authors' model is provided by (18) and not by the combo. We provide a representation of the latter in Fig.5, filtering LTI circuit, as its equivalent model when $f \sim kf_{LO}$ leads to the same approximation as in (18).

C. Matching to source

We will consider $f = kf_{LO}$ for that purpose. The particular condition of matching, useful for mixer-first architectures, implies $Z_{in}^{(k)} = R_a$. By developing the previous equations and applying this additional trend, the value of $R_{L\_match}^{(k)}$ where $R_B^{(k)} = \gamma_N^{(k)}R_{L\_match}^{(k)}$ can be retrieved. At resonance,

$$R_{sw} + R_{sh}^{(k)}\|R_B^{(k)} = R_a \tag{19}$$

that is equivalent to (20).

$$\gamma_N^{(k)}R_{L\_match}^{(k)} = \frac{\alpha_N^{(k)}R'_a\cdot(R_a - R_{sw})}{\alpha_N^{(k)}R'_a - (R_a - R_{sw})} \tag{20}$$

Let's call

$$\rho = \frac{R_{sw}}{R_a} \tag{21}$$

Then

$$R_{L\_match}^{(k)} = R_a\cdot\frac{1}{\gamma_N^{(k)}}\cdot\frac{\alpha_N^{(k)}(1+\rho)\cdot(1-\rho)}{\alpha_N^{(k)}(1+\rho)-(1-\rho)} \tag{22}$$

IV. Filtering and Mixing Responses

A. Filtering gain

For $f \sim kf_{LO}$, filtering voltage gain is given by (23)

$$\left|\frac{V_{in}(f)}{V_{RF}(f)}\right| = \left|\frac{Z_{in}^{(k)}}{R_a + Z_{in}^{(k)}}\right| \tag{23}$$

B. Mixing gain

As aforementioned in (5), $v_{c,n}(t) = i_n(t) * z(t)$ which can be re-written as

$$v_{c,n}(t) = \left[i_{RF}(t)\cdot\left(w_{T_{LO}}\left(t-\frac{nT_{LO}}{N}\right) * \Pi_{\frac{T_{LO}}{N}}(t)\right)\right] * z(t) \tag{24}$$

Fourier transform of $v_{c,n}(t)$ leads to:

$$V_{c,n}(f) = \left[I_{RF}(f) * \left(W_{f_{LO}}(f)\cdot e^{-j2\pi f n\frac{T_{LO}}{N}}\cdot\frac{1}{N}\cdot sinc\left(\pi f\frac{T_{LO}}{N}\right)\right)\right]\cdot Z(f) \tag{25}$$

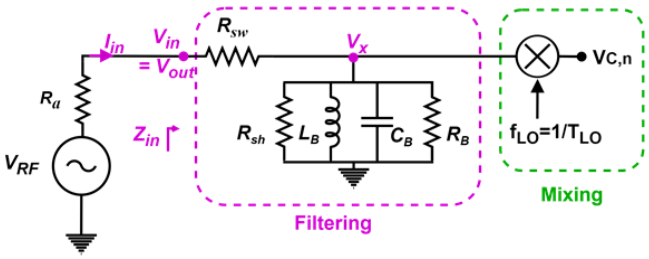

Fig. 5: Representation showing the two functions: filtering and mixing. Filtering LTI model at harmonic k of the LO clock.

By reminding that RF signal is the convolution of baseband signal around f_{RF}, and that $I_{RF}(f) = \frac{V_{RF}(f)}{R'_a}$ then it clearly appears that

$$V_{c,n}(f) = \left[\frac{V_{BB} * \left(\frac{\delta(f-f_{RF})+\delta(f+f_{RF})}{2} \right)}{R'_a} * \left(W_{f_{LO}}(f) \cdot e^{-j2\pi f n \frac{T_{LO}}{N}} \cdot \frac{1}{N} \cdot sinc\left(\pi f \frac{T_{LO}}{N} \right) \right) \right] \cdot Z(f) \tag{26}$$

which can be split in two terms

$$V_{c,n}(f) = \left[\sum_{q=-\infty}^{+\infty} \left\{ \frac{V_{BB} * \delta(f - f_{RF} - qf_{LO})}{2R'_a} \cdot e^{-j2\pi \frac{qn}{N}} \cdot \frac{1}{N} \cdot sinc\left(\frac{q\pi}{N} \right) \right\} + \sum_{p=-\infty}^{+\infty} \left\{ \frac{V_{BB} * \delta(f + f_{RF} - pf_{LO})}{2R'_a} \cdot e^{-j2\pi \frac{pn}{N}} \cdot \frac{1}{N} \cdot sinc\left(\frac{p\pi}{N} \right) \right\} \right] \cdot Z(f) \tag{27}$$

The only part of $V_{c,n}(f)$ spectrum for which $Z(f)$ is non null is for $|f|$ below cutoff frequency, typically $\frac{1}{2\pi C_L (N R'_a \| R_L)}$ for simple high resistive load R_L. For carrier frequencies $f_{RF} \sim k f_{LO}$, this corresponds to the filtering of the spectrum in the low frequencies part in such a way that only the components corresponding to $q = -p = -k$ remains. The corresponding $V_{C,n}$ is referred to as $V_{C,n}^{(k)}$ in (28).

$$V_{c,n}^{(k)}(f) = \frac{1}{R'_a} \left[V_{BB} * \left(\frac{\delta(f - f_{RF} + kf_{LO}) \cdot e^{+j2\pi \frac{kn}{N}}}{2} + \frac{\delta(f + f_{RF} - kf_{LO}) \cdot e^{-j2\pi \frac{kn}{N}}}{2} \right) \right] \cdot \frac{1}{N} sinc\left(\frac{k\pi}{N} \right) \cdot Z(f) \tag{28}$$

By defining $f_{RF} - kf_{LO} = f_{IF}$ as the intermediate frequency, the bracketed text in (28) is the spectral response of $V_{IF,n}^{(k)}(f)$ defined in time domain by (29).

$$v_{IF,n}^{(k)}(t) = A(t) cos\left(2\pi f_{IF} \left(t + \frac{knT_{IF}}{N} \right) + \phi(t) \right) \tag{29}$$

$V_{IF,n}^{(k)}(f)$ is the transposition around $f_{IF} = f_{RF} - kf_{LO}$ of baseband signal, the same way as $V_{RF}(f)$ is the transposition around f_{RF} of baseband signal. Frequency transposition and filtering of baseband signal at IF are illustrated on Fig.3.c. Both $V_{IF,n}^{(k)}(f)$ and $V_{RF}(f)$ present the same modulus as $V_{BB}(f)$. Hence mixing gain is independent from path, as illustrated on Fig.4, and can be written as (30).

$$\left| \frac{V_{c,n}^{(k)}(f)}{V_{RF}(f)} \right| = \left| \frac{1}{R'_a} \cdot \frac{1}{N} sinc\left(\frac{k\pi}{N} \right) \cdot Z(f) \right| \tag{30}$$

If $Z(f)$ is the one of (6).b then

$$\left| \frac{V_{c,n}^{(k)}(f)}{V_{RF}(f)} \right| = \left| \frac{1}{R'_a} \cdot \frac{1}{N} sinc\left(\frac{k\pi}{N} \right) \cdot \frac{N R'_a \| R_L}{1 + j2\pi f C_L (N R'_a \| R_L)} \right| \tag{31}$$

Inherently, the mixing voltage gain does not present the same bandwidth, and attenuation, as the filtering voltage gain, which will be verified in the next section. Note that, if source and load impedances are different from simple resistances, it is enough to change R_a to $R_a \| X_a$ and R_L to $R_L \| X_L$ in the previous equations.

V. Discussion on model validity and accuracy

A. Simulated cases

In order to validate the harmonic model presented so far for both filtering and mixing gains, four cases with ideal components are simulated through harmonic balance (HB), at $f_{LO} = 1$ GHz. For the sake of honesty, authors chose reasonable values for their constant parameters while studying the impact of the varying one, meaning small value of the number of paths $N = 4$, typical antenna impedance $R_a = 50\ \Omega$, lossy switches $R_{sw} = 10\ \Omega$, not so high resistive load $R_L = 1$ kΩ, but kept a capacitive path strong enough, i.e $C_L = 20$ pF, in order to respect the main hypothesis of the model consisting in neglecting the leakage currents flowing to source or load impedances rather than in capacitance. Fig.6 represents the gains-frequency variations with N, all other items being kept equal. Fig.7 concerns C_L influence. Fig.8 focuses interest on various low and high R_L. Finally, Fig.9 checks the antenna source impact on the gains-frequency responses.

CAD HB simulations for RF filtering, in straight lines, have the RF frequency varying continuously from 0.5 to 3.5GHz so that a continuous simulated curve can be observed in Fig.6.a, 7.a, 8.a, 9.a. 200 harmonics are considered for HB. In the mean time, calculations in dashed lines are performed three times where the frequency range representation for each k is chosen in such a way that curve for $k = 2$ cuts curves for $k = 1$ and $k = 3$. This does not occur specifically at $f_{RF} = 1.5$ GHz and $f_{RF} = 2.5$ GHz but in between 1 and 2 GHz or 2 and 3 GHz, respectively.

On the other hand, CAD HB simulations for IF filtering, in straight lines, concern conversion gains and mixing responses, meaning an IF frequency range around the fundamental and its harmonics, leading to the three non-continuous curves in Fig.6.b, 7.b, 8.b, 9.b where the IF frequency range was chosen from 0 to 0.5 GHz in the CAD tool. Calculations with square dots are performed three times: between 0.5 and 1.5 GHz for $k = 1$, between 1.5 and 2.5 GHz for $k = 2$, between 2.5 and 3.5 GHz for $k = 3$.

Some slight discrepancies are expected between simulations and calculations due to the two initial hypotheses. The following subsection discusses the model validity on the basis of those simulated cases. To go further in depth with model accuracy, a specific subsection follows detailing the model errors.

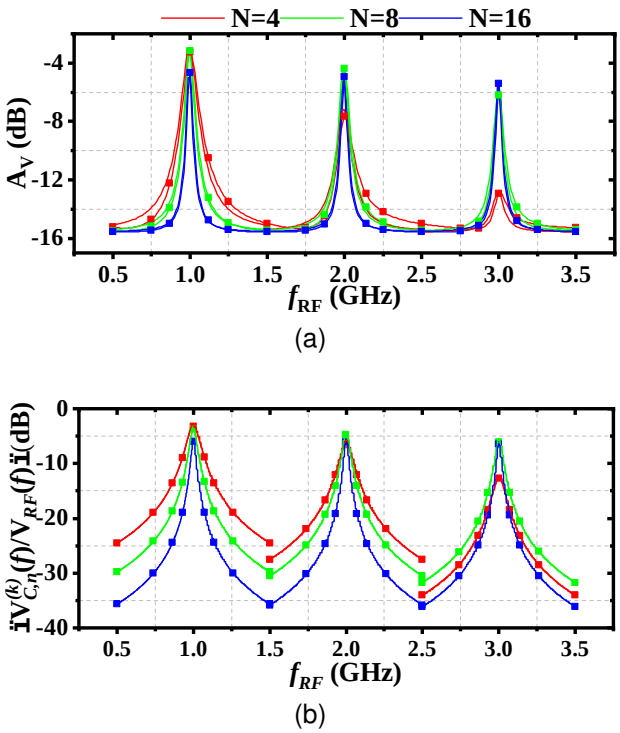

Fig. 6: Analytical (straight) and simulated (square dots) responses versus N. $R_a = 50\ \Omega$, $R_{sw} = 10\ \Omega$, $R_L = 1\ k\Omega$, $C_L = 20$ pF, $f_{LO} = 1$ GHz. a) Filtering voltage gain. b) Mixing voltage gain.

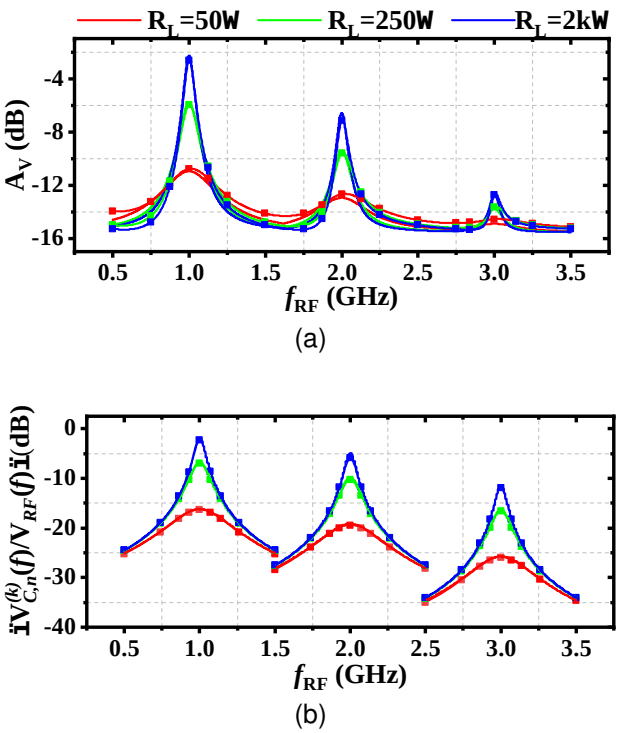

Fig. 8: Analytical (straight) and simulated (square dots) responses versus R_L. $N = 4$, $R_a = 50\ \Omega$, $R_{sw} = 10\ \Omega$, $C_L = 20$ pF, $f_{LO} = 1$ GHz. a) Filtering voltage gain. b) Mixing voltage gain.

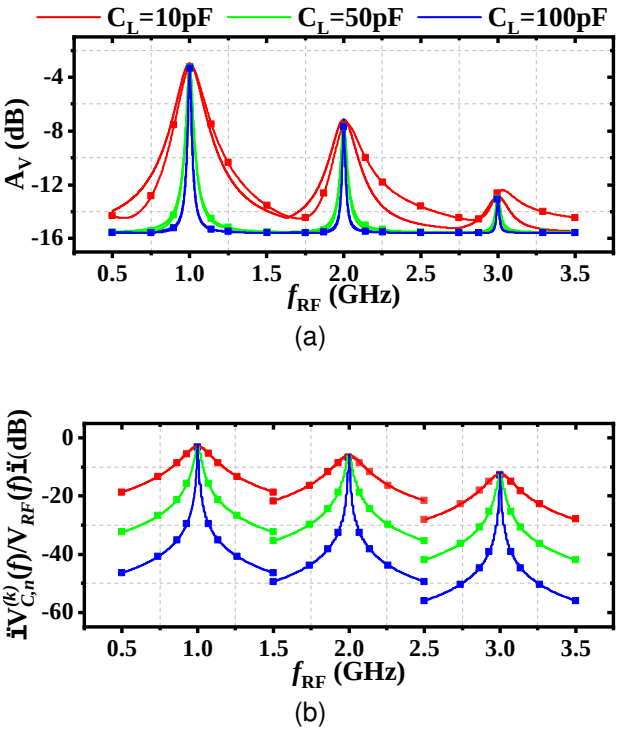

Fig. 7: Analytical (straight) and simulated (square dots) responses versus C_L. $N = 4$, $R_a = 50\ \Omega$, $R_{sw} = 10\ \Omega$, $R_L = 1\ k\Omega$, $f_{LO} = 1$ GHz. a) Filtering voltage gain. b) Mixing voltage gain.

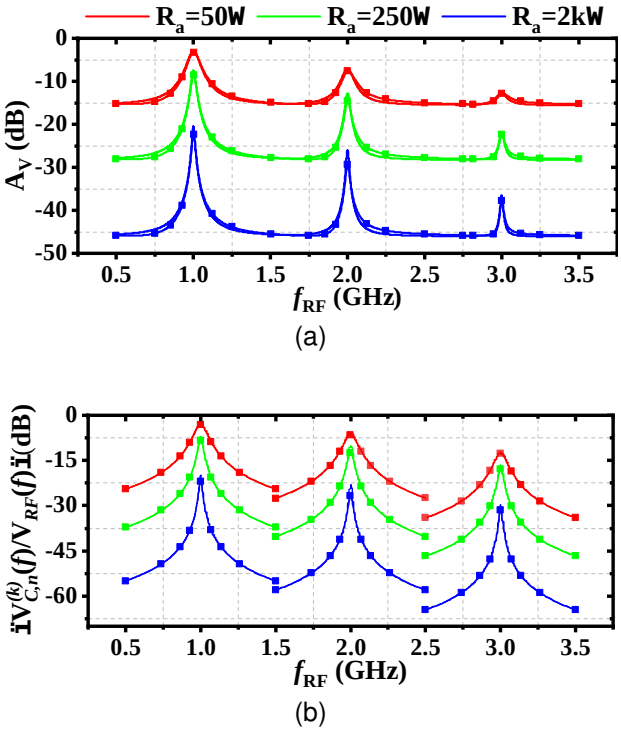

Fig. 9: Analytical (straight) and simulated (square dots) responses versus R_a. $N = 4$, $R_{sw} = 10\ \Omega$, $R_L = 1\ k\Omega$, $C_L = 20$ pF, $f_{LO} = 1$ GHz. a) Filtering voltage gain. b) Mixing voltage gain.

B. Discussion on model validity as compared to simulated cases

In Fig.6, it is noteworthy that, despite the aforementioned approximations, the model fits very well the simulation with the number of path, even for N as small as 4. The model is particularly correct at fundamental and does not exceed 0.4 dB for the second harmonic at $f_{LO} = 2$ GHz. Even if filtering response around kf_{LO} presents higher attenuation as compared to filtering response around f_{LO}, filtering at kf_{LO} is still of high interest because the circuit only needs clock signal at f_{LO} to mix with $f_{RF} \sim kf_{LO}$ whereas some charge pump can act as a passive voltage amplifier, as in [20]. With the considered components values, for small N, filter attenuation might prevent from using the NPF at third harmonic but for big N, it is interesting to discuss the compromise between surface on the die and the reduced consumption of the VCO by a factor of 3.

Fig.7 typically illustrates the impact of the capacitive path. For extremely high values of C_L, model perfectly suits the simulation, but for capacitances values in the order of 10 pF, where $f_{LO} = 1$ GHz, it differs further and further from it when the considered harmonic increases. This is due to the influence of other components on the current charge of the capacitor. Despite a lack of accuracy in the model, this observation is of importance when considering integration: low capacitances, already sensitive to mismatch, might lead to bandwidth even more sensitive to the mismatch of other components.

In Fig.8, it appears that the constraints of the load impedance are somewhat nonexistent for model validity. In practice, low R_L leads to increased losses and poor filtering and mixing voltage gains. Finally, Fig.9 shows the impact of source impedance on attenuation: higher I_{RF} is reached and so higher gain is demonstrated when R_a is small. Besides, even for low R_a, due to the strong value of $\alpha_N^{(k)}$, R_{sh} is sufficiently high not to impact filtering gain or bandwidth.

C. Model accuracy: the capacitance value trade-off

The proposed model relies on two main hypotheses: 1) for charging purposes, it is assumed a strong capacitive RF path through C_L, that is, i) $\frac{1}{\omega C_L} \ll R_L$ which is usually the case for high input impedance buffers; and ii) $\frac{1}{\omega C_L} \ll R'_a$, which may be hard to implement for low-impedance antenna sources, and 2) for discharging purposes, it is assumed that the discharge time of C_L in R'_a during the time slot $\frac{T_{LO}}{N}$ is fast, that is, $R'_a C_L \ll \frac{T_{LO}}{N}$. By considering the most constraining condition for charging, and focusing on harmonic k, these two assumptions can be expressed as,

$$\frac{1/\omega_{LO} C_L}{R'_a} \ll k \tag{32}$$

$$\frac{1/\omega_{LO} C_L}{R'_a} \gg \frac{N}{2\pi} \tag{33}$$

Complying with both (32) and (33) requires a trade-off. In this work, for simplicity, we propose $\frac{1/\omega_{LO} C_L}{R'_a} = 1$, that is particularizing in a capacitance value C_L of 3.2 pF for $f_{LO} = 1$ GHz, a null R_{sw} and $R_a = 50\ \Omega$. The model is expected to provide the best accuracy for this value of C_L, and deviate from the observed behavior as we move away from it. In other words, for filtering purposes, this value is expected to ensure the best compromise between charging and discharging time of the N-path if the designer targets an RLC-like behavior, i.e. the most symmetrical as possible around f_{LO}. The objective is different when dealing with N-path mixer: in order to get high conversion gain, it is of major importance to charge C_L during $\frac{T_{LO}}{N}$ with the highest available current, which is facilitated by much higher capacitance values than the proposed trade-off. Typically with the previous data, a capacitance of 32 pF can be a good choice.

In order to quantify the model accuracy and to validate the initial conditions, two error functions are proposed. For both A_v and G_c, σ_{error} is the relative error between the maximum calculated voltage gain and the maximum simulated voltage gain. ϵ_{error} is the maximum relative error between the simulated and calculated low cut-off frequency, f_l, and between the simulated and calculated high cut-off frequencies, f_h:

$$\begin{aligned}
A_v\,\sigma_{error} &= \frac{|A_v|^{sim}_{max} - |A_v|^{cal}_{max}}{|A_v|^{sim}_{max}} \quad (a)\\
G_c\,\sigma_{error} &= \frac{|G_c|^{sim}_{max} - |G_c|^{cal}_{max}}{|G_c|^{sim}_{max}} \quad (b)\\
A_v\,\epsilon_{error} &= max\left(\frac{f^{sim}_{l,A_v} - f^{cal}_{l,A_v}}{f^{sim}_{l,A_v}}; \frac{f^{sim}_{h,A_v} - f^{cal}_{h,A_v}}{f^{sim}_{h,A_v}}\right) \quad (c)\\
G_c\,\epsilon_{error} &= max\left(\frac{f^{sim}_{l,G_c} - f^{cal}_{l,G_c}}{f^{sim}_{l,G_c}}; \frac{f^{sim}_{h,G_c} - f^{cal}_{h,G_c}}{f^{sim}_{h,G_c}}\right) \quad (d)
\end{aligned} \tag{34}$$

First, we consider ϵ_{error}. For any values of the harmonic components, any A_v, G_c, and any C_L within a range of two decades over the proposed trade-off value and two decades below, $\epsilon_{error} < 2\%$. This is true as long as a cut-off frequency is observable. For example, no cut-off can be defined for the third harmonic in Fig. 7.a. In that case, it can be simply stated that the N-path filter does not work anymore. Second, Fig.10 and Fig.11 provide σ_{error} as a function of C_L by considering for *x-axis* the ratio $\frac{1/k.\omega_{LO} C_L}{R'_a}$ where $k = 1$ for Fig.10 and $k = 3$ for Fig.11. As can be observed in all the curves of Fig.10 and Fig.11, there is a minimum in the model error, which can be explained by the trade-off between (32) and (33). Obviously, for very low C_L (right part of the hollow-like curves), the error increases drastically due to charge phenomena and for very high C_L (i.e., low values in the *x-axis*), the error increases due to discharge phenomena. In Fig.10.a, a minimum error around 1% is reached for a ratio of 0.8, that is close to our proposition of 1 for $R'_a = 50\ \Omega$. The minimum error deviates from this location when increasing R'_a, since the need for high C_L becomes significant, underlining the importance of the charging hypothesis. Additionally, it is observed that the model error increases with R'_a, reaching up to 22% when $R'_a = R_L = 1$ kΩ. This observation emphasizes the impact of the discharge phenomena, that so far has been rarely considered when dealing with N-paths. Concerning the third harmonic in

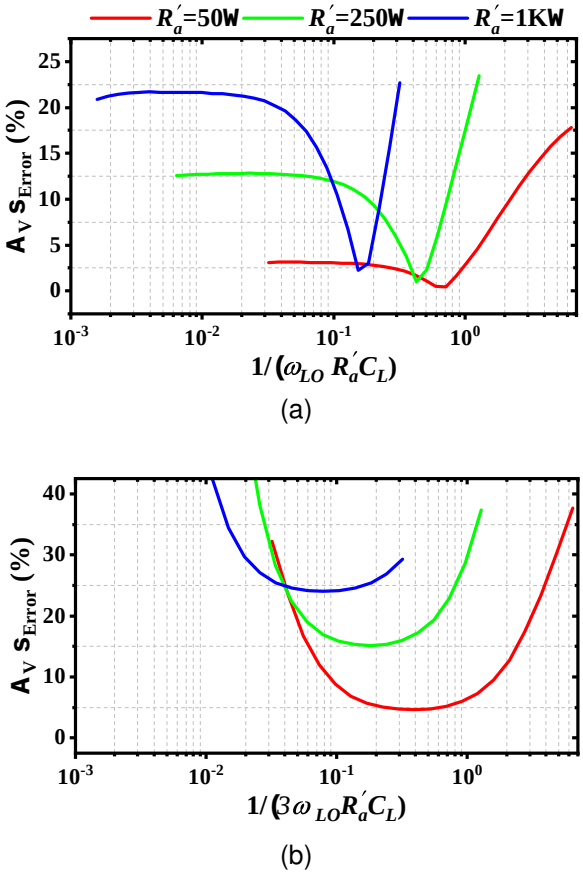

Fig. 10: Filtering voltage gain error function. a) At fundamental. b) At third harmonic. $N = 4$, $R_a = 50\ \Omega$, $R_{sw} = 0\ \Omega$, $R_L = 1\ k\Omega$, $f_{LO} = 1$ GHz, C_L varies.

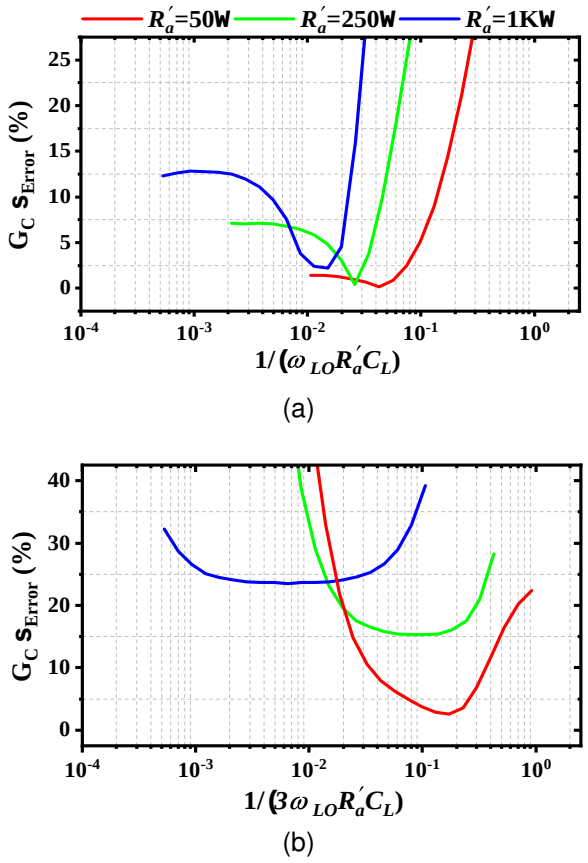

Fig. 11: Mixing voltage gain error function. a) At fundamental. b) At third harmonic. $N = 4$, $R_a = 50\ \Omega$, $R_{sw} = 0\ \Omega$, $R_L = 1\ k\Omega$, $f_{LO} = 1$ GHz, C_L varies.

Fig.10.b, the observations are qualitatively similar, with a shift towards higher trade-off capacitances (with a ratio of 3) but also higher minimum errors and a more pronounced impact of the discharge phenomena. Nevertheless, the error stays inferior to 25% for a large range of R_a' from 50 Ω to 1 kΩ and for a ratio $\frac{1/k.\omega_{LO}C_L}{R_a'}$ from 0.04 to 0.2, which is already interesting for an analytical pre-design.

As for mixing conversion gain in Fig.11, there exists also a trade-off but it is noteworthy that the impact of the charge phenomena is much more significant with minimum $G_c\,\sigma_{error}$ obtained for $\frac{1/\omega_{LO}C_L}{R_a'}$ ranging from 0.01 to 0.04. Concerning the second harmonic, it has not been shown in the figures for the sake of conciseness, as it presents a similar behavior in between $k = 1$ and $k = 3$.

VI. Validation through Measurements

A. Design implementation

In order to better depict the scope of this study, an NPF-NPM structure has been implemented and measured. The circuit components are chosen in order to minimize the mean model error over all the harmonics, for both filtering voltage gain, A_v, and mixing voltage gain, G_c. As a matter of fact, only the A_v and G_c will be provided without any comparison with the state-of-the-art of the other characteristics, although components choices were driven by non-linearity, power consumption and noise considerations. The clock frequency is set to 0.5 GHz. The source from instrument tool will provide a 50-Ω impedance. In the technology at hand, Global Foundry 45RFSOI, the switches present a resistance R_{sw} of 15 Ω, corresponding to a gate width of 10 μm, a median value that maintains an optimal balance between noise figure and energy consumption. The MOM capacitance presents a bottom plate at M2 level, leading to a shunt parasitic capacitance of only 10% of its nominal value. The choice of $C_L = 25$ pF appears to be a good compromise for illustrating the model accuracy as $\frac{1/k.\omega_{LO}C_L}{R_a'}$ is equal to 0.2 for $k = 1$, 0.1 for $k = 2$ and 0.065 for $k = 3$.

The implemented circuit is shown in Fig.12. It includes a 25% Windmill frequency divider as in [24]. The latter is interesting as it uses only one NOR gate buffer per phase to minimize power consumption and phase noise. When compared to state-of-the-art designs as detailed in [24], it requires half the power consumption and has 2-dB less phase noise. To measure the scattering parameters in a 50-Ω environment, a single-stage "unity-gain" buffer is added at the output. In practice, buffer shows a 1.8-dB gain, simulated at post-layout simulation levels. For practical measurements,and after deembedding, the buffer allows S_{21} to accurately represent the mixing voltage gain of the structure when used with a

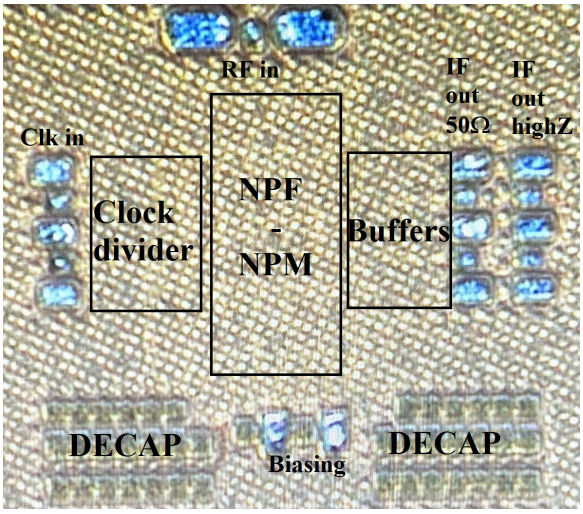

Fig. 12: Implemented circuit in Global Foundry 45RFSOI. $N = 4$, $R_a = 50\ \Omega$, $R_{sw} = 15\ \Omega$, high-Z $R_L = 1$ from buffers, $C_L = 25$ pF, $f_{LO} = 0.5$ GHz.

high-impedance output node.

B. Measurement results

All small-signal S-parameters measurements are performed via on-wafer probing using an Anritsu 2-port MS4640B series Vector Network Analyzer (VNA). Fig.13 compares the calculated, simulated with ideal components, simulated with PDK and measured A_V and G_c. The calculated results are obtained from (23) and (31). Calculus is performed three times to plot the response around the three targeted harmonics: 0.5 GHz, 1 GHz and 1.5 GHz. The CAD HB simulations are considering 200 harmonics. For A_v, they have the RF frequency varying continuously from 0.25 to 1.75 GHz so that a continuous simulated curve can be observed in Fig.13.a. For G_c, IF frequency ranges from 0 to 0.25 GHz around the fundamental and its harmonics, leading to the three non-continuous curves in Fig.13.b. Measurements are fully extracted from small-signal S-parameters. Measured S_{11} enables to derive the ratio V_{in}/V_{RF} that is A_v. Measured S_{21} with 50-Ω ports is first deembedded from buffer voltage gain. Then, thanks to A_v, the ratio $V_{c,n}/V_{RF}$ that is exactly G_c can be extracted. Fig.13.a and b show a very good prediction of the model as compared to ideal simulation. Also, the maturity of the technology proves excellent agreement between ideal simulation, PDK simulation and measurements. Due to probes limitations, measurements were conducted only up to 1.2 GHz, restricting model comparison to the two first harmonics only. Table I summarizes the errors between model and other plots.

TABLE I: MODEL ERROR FOR FIG.13.A AND B.

$\sigma_{error}(\%)$	A_v			G_c		
	$k=1$	$k=2$	$k=3$	$k=1$	$k=2$	$k=3$
Ideal sim.	0.15	0.04	1.33	0.02	2.99	6.85
PDK sim.	1.70	2.36	0.53	0.08	2.99	11.17
Meas	5.51	10.49	NA	0.96	2.43	NA

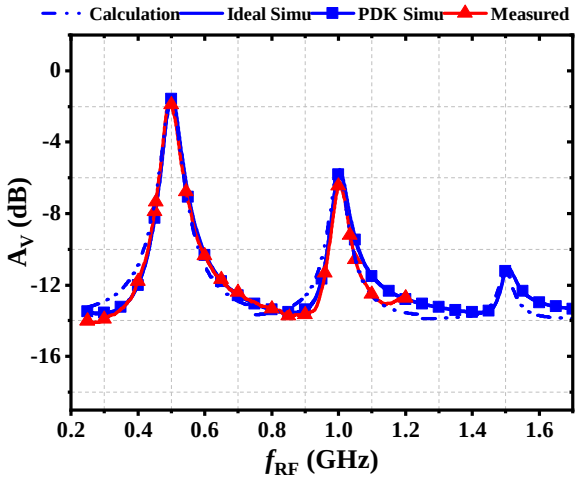

(a)

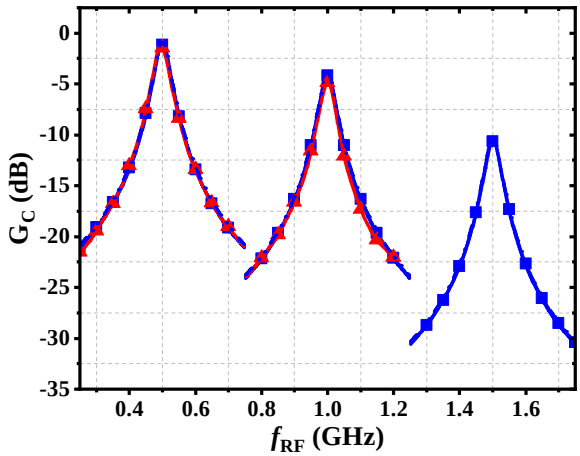

(b)

Fig. 13: Measured, simulated with ideal components, simulated with PDK and calculated through model responses. a) Filtering voltage gain. b) Mixing voltage gain. $N = 4$, $R_a = 50\ \Omega$, $R_{sw} = 15\ \Omega$, high-Z R_L from buffers, $C_L = 25$ pF, $f_{LO} = 0.5$ GHz.

VII. Conclusion

In this work, a general approach to accurately model N-path filters and mixers has been proposed. The model considers the impact of both source and load impedances. Thanks to a frequency-domain analysis based on the Fourier transform, we were able to derive for the first time a set of mathematical equations to accurately describe the behavior of the filtering and mixing voltage gains around each harmonic component of the LO clock. The filtering voltage gain is calculated from (23), with the help of (15), (16) and (18), while the mixing voltage gain is calculated from (31). If source and load impedances are different from simple resistances, it is enough to change R_a to $R_a \| X_a$ and R_L to $R_L(f) \| X_L(f)$ in the previous equations. The analysis has been validated on the basis of simple R_a and R_L, showing the limits of the

model in terms of a maximum targeted error on the filtering and mixing functions within a specific range of capacitive paths values. As a proof-of-concept, an NPF-NPM has been implemented and characterized in the laboratory. Measurement results are in good agreement with the analytical model for both fundamental and second harmonic, with an error less than 10.5%.

APPENDICES

A. Proof for (9) from (7) and (8)

From (7) and (8), it comes for $v_x(t)$ in time domain

$$\begin{aligned} v_x(t) = \sum_{n=0}^{N-1} \Bigg\{ \Bigg[\Bigg(i_{RF}(t) \cdot \Bigg(w_{T_{LO}} \left(t - \frac{nT_{LO}}{N} \right) \\ * \Pi_{\frac{T_{LO}}{N}}(t) \Bigg) \Bigg) * z(t) \Bigg] \\ \cdot \left[w_{T_{LO}} \left(t - \frac{nT_{LO}}{N} \right) * \Pi_{\frac{T_{LO}}{N}}(t) \right] \Bigg\} \end{aligned} \tag{35}$$

In frequency domain, this leads to

$$\begin{aligned} V_x(f) = \sum_{n=0}^{N-1} \Bigg\{ \Bigg[\Bigg(I_{RF}(f) * \Bigg(W_{f_{LO}}(f) \cdot e^{-j2\pi f n \frac{T_{LO}}{N}} \\ \cdot \frac{1}{N} \cdot sinc \left(\pi f \frac{T_{LO}}{N} \right) \Bigg) \Bigg) \cdot Z(f) \Bigg] \\ * \left[W_{f_{LO}}(f) \cdot e^{-j2\pi f n \frac{T_{LO}}{N}} \cdot \frac{1}{N} \cdot sinc \left(\pi f \frac{T_{LO}}{N} \right) \right] \Bigg\} \end{aligned} \tag{36}$$

that can be written in a more explicit way by

$$\begin{aligned} V_x(f) = \sum_{n=0}^{N-1} \Bigg\{ \Bigg[\sum_{q=-\infty}^{+\infty} \Bigg(I_{RF}(f - qf_{LO}) \cdot e^{-j2\pi \frac{qn}{N}} \\ \cdot \frac{1}{N} \cdot sinc \left(\frac{q\pi}{N} \right) \Bigg) \cdot Z(f) \Bigg] \\ * \left[W_{f_{LO}}(f) \cdot e^{-j2\pi f n \frac{T_{LO}}{N}} \cdot \frac{1}{N} \cdot sinc \left(\pi f \frac{T_{LO}}{N} \right) \right] \Bigg\} \end{aligned} \tag{37}$$

or even more explicit

$$\begin{aligned} V_x(f) = \sum_{n=0}^{N-1} \Bigg\{ \sum_{k=-\infty}^{+\infty} \Bigg[\sum_{q=-\infty}^{+\infty} (I_{RF}(f - qf_{LO} - kf_{LO}) \\ \cdot e^{-j2\pi \frac{qn}{N}} \cdot \frac{1}{N} \cdot sinc \left(\frac{q\pi}{N} \right) \Bigg) \cdot Z(f - kf_{LO}) \\ \cdot e^{-j2\pi \frac{kn}{N}} \cdot \frac{1}{N} \cdot sinc \left(\frac{k\pi}{N} \right) \Bigg] \Bigg\} \end{aligned} \tag{38}$$

By inverting the summations

$$\begin{aligned} V_x(f) = \sum_{k=-\infty}^{+\infty} \Bigg[\sum_{q=-\infty}^{+\infty} (I_{RF}(f - qf_{LO} - kf_{LO}) \\ \cdot \frac{1}{N} \cdot sinc \left(\frac{q\pi}{N} \right) \cdot \frac{1}{N} \cdot sinc \left(\frac{k\pi}{N} \right) \cdot Z(f - kf_{LO}) \\ \cdot \sum_{n=0}^{N-1} \left\{ e^{-j2\pi \frac{qn}{N}} \cdot e^{-j2\pi \frac{kn}{N}} \cdot \right\} \Bigg) \Bigg] \end{aligned} \tag{39}$$

The sum on n is non-null only for $q = mN - k$ with m a relative integer. Also $V_x(f)$ is non-null for $f \sim kf_{LO}$ due to $Z(f - kf_{LO})$. Let's focus on frequency $f = kf_{LO}$; the identification of the component kf_{LO} of $V_x(f)$, that is to say $V_x(kf_{LO})$ with the corresponding component of $I_{RF}(kf_{LO} - qf_{LO} - kf_{LO})$ leads to $q = -k$ as the unique solution. Finally, (9) is proven.

$$V_x(f) = \sum_{k=-\infty}^{+\infty} \left[I_{RF}(f) \cdot \frac{N}{N^2} \cdot sinc^2 \left(\frac{k\pi}{N} \right) \cdot Z(f - kf_{LO}) \right] \tag{40}$$

B. Proof for (18) from (16) and (17)

As a reminding, when $Z(f)$ is the basic impedance of (6), then:

$$\begin{aligned} Z_{in}^{(k)} = R_{sw} + \\ \frac{\gamma_N^{(k)} \cdot N R'_a R_L}{N R'_a + R_L + j2\pi\Delta f \cdot N R'_a C_L R_L - \gamma_N^{(k)} \cdot N R_L} \end{aligned} \tag{41}$$

By naming

$$R_B^{(k)} = \gamma_N^{(k)} R_L \tag{42}$$

Then, $Z_{in}^{(k)}$ comes to

$$\begin{aligned} Z_{in}^{(k)} = R_{sw} + \\ + \frac{N R'_a R_B^{(k)}}{\left(N R'_a + \frac{R_B^{(k)}}{\gamma_N^{(k)}} - N R_B^{(k)} \right) + j2\pi\Delta f \cdot N R'_a \frac{1}{\gamma_N^{(k)}} C_L \cdot R_B^{(k)}} \end{aligned} \tag{43}$$

which can be arranged as follows:

$$\begin{aligned} Z_{in}^{(k)} = R_{sw} + \\ + \frac{N R'_a R_B^{(k)}}{\left(N R'_a + \frac{1 - N\gamma_N^{(k)}}{\gamma_N^{(k)}} R_B^{(k)} \right) + j2\pi\Delta f \cdot N R'_a \frac{1}{\gamma_N^{(k)}} C_L \cdot R_B^{(k)}} \end{aligned} \tag{44}$$

Let's call

$$\begin{aligned} C_B^{(k)} &= \frac{C_L}{2\gamma_N^{(k)}} \\ R_{sh}^{(k)} &= \alpha_N^{(k)} R'_a \\ \alpha_N^{(k)} &= \frac{N\gamma_N^{(k)}}{1 - N\gamma_N^{(k)}} \end{aligned} \tag{45}$$

We can now re-write $Z_{in}^{(k)}$

$$Z_{in}^{(k)} = R_{sw} + \frac{R_{sh}^{(k)} \cdot R_B^{(k)}}{\left(R_B^{(k)} + R_{sh}^{(k)} \right) + j2\pi \cdot 2\Delta f \cdot C_B^{(k)} R_{sh}^{(k)} \cdot R_B^{(k)}} \tag{46}$$

or more explicitly the harmonic-dependant impedance of (18).

$$Z_{in}^{(k)} = R_{sw} + \frac{R_{sh}^{(k)} \| R_B^{(k)}}{1 + j2\pi \cdot 2\Delta f \cdot C_B^{(k)} \left(R_{sh}^{(k)} \| R_B^{(k)} \right)} \tag{47}$$

REFERENCES

[1] C. Andrews and A. C. Molnar, "A Passive Mixer-First Receiver With Digitally Controlled and Widely Tunable RF Interface," in *IEEE Journal of Solid-State Circuit*, vol. 45, no. 12, pp. 2696-2708, Dec. 2010, doi: 10.1109/JSSC.2010.2077151.

[2] M. C. M. Soer, E. A. M. Klumperink, P. -T. de Boer, F. E. van Vliet and B. Nauta, "Unified Frequency-Domain Analysis of Switched-Series-RC Passive Mixers and Samplers," in *IEEE Transactions on Circuits and Systems I: Regular Papers*, vol. 57, no. 10, pp. 2618-2631, Oct. 2010, doi: 10.1109/TCSI.2010.2046968.

[3] C. Salazar, A. Cathelin, A. Kaiser, et J. Rabaey, "A 2.4 GHz Interferer-Resilient Wake-Up Receiver Using a Dual-IF Multi-Stage N-Path Architecture," in *IEEE Journal of Solid-State Circuits*, vol. 51, no 9, pp. 2091-2105, Sept. 2016, doi: 10.1109/JSSC.2016.2582509.

[4] H. Shao, P. I. Mak, G. Qi and R. P. Martins, "A 266$-\mu$W Bluetooth Low-Energy (BLE) Receiver Featuring an N Path Passive Balun LNA and a Pipeline Down-Mixing BB Extraction Scheme Achieving 77 $-$ dB SFDR and $-3 - dBmOOB - B - 1dB$," in *IEEE Journal of Solid State Circuits*, vol. 57, no. 12, pp. 3669-3680, Dec. 2022, doi: 10.1109/JSSC.2022.3200932.

[5] Z. Ru, N. A. Moseley, E. A. M. Klumperink and B. Nauta, "Digitally Enhanced Software-Defined Radio Receiver Robust to Out-of-Band Interference," in *IEEE Journal of Solid State Circuits*, vol. 44, no. 12, pp. 3359-3375, Dec. 2009, doi: 10.1109/JSSC.2009.2032272.

[6] R. Bagheri et al., "An 800-MHz–6-GHz Software-Defined Wireless Receiver in 90-nm CMOS," in *IEEE Journal of Solid State Circuits*, vol. 41, no. 12, pp. 2860-2876, Dec. 2006, doi: 10.1109/JSSC.2006.884835.

[7] R. van de Beek, J. Bergervoet, H. Kundur, D. Leenaerts and G. van der Weide, "A 0.6-to-10GHz Receiver Front-End in 45nm CMOS," *2008 IEEE International Solid-State Circuits Conference - Digest of Technical Papers*, San Francisco, CA, USA, 2008, pp. 128-601, doi: 10.1109/ISSCC.2008.4523090.

[8] F. Lin, P. -I. Mak and R. P. Martins, "An RF-to-BB-Current-Reuse Wideband Receiver With Parallel N-Path Active/Passive Mixers and a Single-MOS Pole-Zero LPF," in *IEEE Journal of Solid State Circuits*, vol. 49, no. 11, pp. 2547-2559, Nov. 2014, doi: 10.1109/JSSC.2014.2354647.

[9] Y. -C. Lien, E. A. M. Klumperink, B. Tenbroek, J. Strange and B. Nauta, "Enhanced-Selectivity High-Linearity Low-Noise Mixer-First Receiver With Complex Pole Pair Due to Capacitive Positive Feedback," in *IEEE Journal of Solid State Circuits*, vol. 53, no. 5, pp. 1348-1360, May 2018, doi: 10.1109/JSSC.2018.2791490.

[10] Y. -C. Lien, E. A. M. Klumperink, B. Tenbroek, J. Strange and B. Nauta, "High-Linearity Bottom-Plate Mixing Technique With Switch Sharing for N -path Filters/Mixers," in *IEEE Journal of Solid State Circuits*, vol. 54, no. 2, pp. 323-335, Feb. 2019, doi: 10.1109/JSSC.2018.2878812.

[11] Y. Xu, J. Zhu and P. R. Kinget, "A Blocker-Tolerant RF Front End With Harmonic-Rejecting N -Path Filter," in *IEEE Journal of Solid State Circuits*, vol. 53, no. 2, pp. 327-339, Feb. 2018, doi: 10.1109/JSSC.2017.2778273.

[12] A. A. Shakoush, E. Lauga-Larroze, F. Podevin, S. Ibrahim, L. Fesquet and S. Bourdel, "Improved π-Delayed Harmonic Rejection N-Path Mixer for Low Power Consumption and Multistandard Receiver," *2020 18th IEEE International New Circuits and Systems Conference (NEWCAS)*, Montreal, QC, Canada, 2020, pp. 170-173, doi: 10.1109/NEWCAS49341.2020.9159792.

[13] A. Al Shakoush et al., "N-Path Mixer with Wide Rejection Including the 7th Harmonic for Low Power Multi-standard Receivers," *2022 20th IEEE Interregional NEWCAS Conference (NEWCAS)*, Quebec City, QC, Canada, 2022, pp. 256-260, doi: 10.1109/NEWCAS52662.2022.9901392.

[14] C. Andrews and A. C. Molnar, "Implications of Passive Mixer Transparency for Impedance Matching and Noise Figure in Passive Mixer-First Receivers," in *IEEE Transactions on Circuits and Systems I: Regular Papers*, vol. 57, no. 12, pp. 3092-3103, Dec. 2010, doi: 10.1109/TCSI.2010.2052513.

[15] D. Yang, C. Andrews and A. Molnar, "Optimized Design of N-Phase Passive Mixer-First Receivers in Wideband Operation," in *IEEE Transactions on Circuits and Systems I: Regular Papers*, vol. 62, no. 11, pp. 2759-2770, Nov. 2015, doi: 10.1109/TCSI.2015.2479035.

[16] A. Ghaffari, E. A. M. Klumperink, M. C. M. Soer and B. Nauta, "Tunable High-Q N-Path Band-Pass Filters: Modeling and Verification," in *IEEE Journal of Solid State Circuits*, vol. 46, no. 5, pp. 998-1010, May 2011, doi: 10.1109/JSSC.2011.2117010.

[17] E. Klumperink and B. Nauta. "N-Path Filters and Mixer-First Receivers–A Review." *IC Design Insights-from Selected Presentations at CICC 2017*, pp. 221-264.

[18] A. Mirzaei, H. Darabi and D. Murphy, "Architectural Evolution of Integrated M-Phase High-Q Bandpass Filters," in *IEEE Transactions on Circuits and Systems I: Regular Papers*, vol. 59, no. 1, pp. 52-65, Jan. 2012, doi: 10.1109/TCSI.2011.2161370.

[19] G. Han and P. R. Kinget, "Comments on "Architectural Evolution of Integrated M-Phase High-Q Bandpass Filters"," in *IEEE Transactions on Circuits and Systems I: Regular Papers*, vol. 68, no. 1, pp. 550-552, Jan. 2021, doi: 10.1109/TCSI.2020.3029795.

[20] S. Weinreich and B. Murmann, "A 0.6–1.8-mW 3.4-dB NF Mixer-First Receiver With an N-Path Harmonic-Rejection Transformer-Mixer," in *IEEE Journal of Solid State Circuits*, vol. 58, no. 6, pp. 1508-1518, June 2023, doi: 10.1109/JSSC.2022.3214226.

[21] A. Abbasi, A. H. Moshrefi and F. Nabki, "A Wideband Low-Power Current-Reuse RF-to-BB Receiver Using a Clock Strategy Technique," in *2022 20th IEEE Interregional NEWCAS Conference (NEWCAS)*, Quebec City, QC, Canada, 2022, pp. 275-279, doi: 10.1109/NEWCAS52662.2022.9842165.

[22] J. G. Kroapik and M. Salehi, *Digital Communications*, 5^{th} edition. McGraw-Hill Higher Education, 2008, pp. 24-25.

[23] G. Boudoin *et al.*, *Radiocommunications numériques : principes, modélisation et simulation*, 2^{nd} edition, Tome 1. Dunod, 2013.

[24] B. J. Thijssen, E. A. Klumperink, P. Quinlan, and B. Nauta, "2.4-GHz highly selective IoT receiver front end with power optimized LNTA, frequency divider, and baseband analog FIR filter," in *IEEE journal of solid-state circuits*, vol. 56, no. 7, pp. 2007–2017, July 2021, doi: 10.1109/JSSC.2020.3031493.